Since January 2020 Elsevier has created a COVID-19 resource centre with free information in English and Mandarin on the novel coronavirus COVID-19. The COVID-19 resource centre is hosted on Elsevier Connect, the company's public news and information website.

Biosensors and Bioelectronics 202 (2022) 113975

Contents lists available at ScienceDirect

Biosensors and Bioelectronics

journal homepage: www.elsevier.com/locate/bios

Capacitive biosensor based on vertically paired electrodes for the detection of SARS-CoV-2

Jun-Hee Park [a], Ga-Yeon Lee [a,b], Zhiquan Song [a], Ji-Hong Bong [a], Young Wook Chang [a], Sungbo Cho [c], Min-Jung Kang [d], Jae-Chul Pyun [a,*]

[a] Department of Materials Science and Engineering, Yonsei University, 50 Yonsei-Ro, Seodaemun-Gu, Seoul, 03722, South Korea
[b] Electronic Convergence Division, Korea Institute of Ceramic Engineering and Technology (KICET), Jinju, 52851, South Korea
[c] Department of Electronic Engineering, Gachon University, Seongnam-si, Gyeonggi-do, 13120, South Korea
[d] Korea Institute of Science and Technology (KIST), Seoul, South Korea

ARTICLE INFO

Keywords:
Capacitive biosensor
SARS-CoV-2
Vertically paired electrode
PEDOT:PSS
Nucleoprotein (NP)
Immunoassay

ABSTRACT

Vertically paired electrodes (VPEs) with multiple electrode pairs were developed for the enhancement of capacitive measurements by optimizing the electrode gap and number of electrode pairs. The electrode was fabricated using a conductive polymer layer of PEDOT:PSS instead of Ag and Pt metal electrodes to increase the VPE fabrication yield because the PEDOT:PSS layer could be effectively etched using a reactive dry etching process. In this study, sensitivity enhancement was realized by decreasing the electrode gap and increasing the number of VPE electrode pairs. Such an increase in sensitivity according to the electrode gap and the number of electrode pairs was estimated using a model analyte for an immunoassay. Additionally, a computer simulation was performed using VPEs with different electrode gaps and numbers of VPE electrode pairs. Finally, VPEs with multiple electrode pairs were applied for SARS-CoV-2 nucleoprotein (NP) detection. The capacitive biosensor based on the VPE with immobilized anti-SARS-CoV-2 NP was applied for the specific detection of SARS-CoV-2 in viral cultures. Using viral cultures of SARS-CoV-2, SARS-CoV, MERS-CoV, and CoV-strain 229E, the limit of detection (LOD) was estimated to satisfy the cutoff value (dilution factor of 1/800) for the medical diagnosis of COVID-19, and the assay results from the capacitive biosensor were compared with commercial rapid kit based on a lateral flow immunoassay.

1. Introduction

Capacitive biosensors have been developed for non-labeled target analyte detection. The binding of analytes using the specific interactions between antigens and antibodies induced quantitative capacitive changes on the capacitive biosensors according to the bound analyte amount (Chen et al. 2019, 2020; Tang et al., 2014). Such capacitive biosensors frequently use interdigitated electrodes (IDEs) as transducers with immobilized antibodies against target analytes (Jung et al., 2014; Kim et al., 2021; Lee et al., 2018a; Luka et al., 2019; Park et al., 2021; Quoc et al., 2019). The capacitance (C) measured from IDEs had the relation $C = \varepsilon \cdot N \cdot A/d$, where ε represents the permittivity constant, N represents the number of electrode pairs (for a single electrode pair, N=1), A represents the electrode area, and d represents the electrode gap. As IDEs consisted of multiple electrode pairs, the structure was regarded as parallel-connected capacitors (Santos-Neto et al., 2021). Based on this relation, the capacitive biosensor sensitivity based on IDEs is proportional to the electrode area, the number of electrode pairs, and 1/electrode gap (Ghobaei Namhil et al., 2019; Hadiyan et al., 2020; Jung et al., 2014; Lee et al., 2018b; Sathya et al., 2019; Singh et al., 2011). The IDEs were fabricated using lab-based photolithography technology, and the electrode gap (d) was reported to be decreased to a few micrometers (Fowler et al., 2009; Li et al., 2017). For the fabrication of IDEs with an electrode gap (d) of less than a few micrometers, expensive processes are required, such as stepper and focused ion beam (FIB) processes (Ahn et al., 2011; Santschi et al., 2006).

Recently, vertically paired electrodes (VPEs) have been developed to effectively reduce the electrode gap and increase the capacitive biosensor sensitivity (Jung et al., 2014; Lee et al. 2013, 2016, 2018b; Sathya et al., 2019). The vertically paired electrode (VPE) consists of pairs of stacked electrodes and dielectric layers. The VPE was fabricated via (1) sequential deposition of electrodes and parylene film as a

* Corresponding author.
E-mail address: jcpyun@yonsei.ac.kr (J.-C. Pyun).

https://doi.org/10.1016/j.bios.2022.113975
Received 27 September 2021; Received in revised form 31 December 2021; Accepted 6 January 2022
Available online 8 January 2022

dielectric layer between electrodes and (2) etching to expose the vertically layered electrodes (Ghobaei Namhil et al., 2019; Lee et al. 2013, 2018b; Minh et al., 2017). The electrode gap of VPE could be effectively reduced to several hundred nanometers by controlling the thickness of dielectric layer between the electrodes. In this work, parylene film was used as a dielectric layer, which could be controlled to have a thickness of less than 1 μm by thermal deposition (Kim et al., 2020; Song et al., 2021). The capacitance measured from the VPE had also the relation $C = \varepsilon \cdot N \cdot A/d$, where N represents the number of electrode pairs (N≠1), d represents the electrode gap, which is defined by the parylene film thickness. Using the VPE, the capacitive measurement sensitivity based on the specific interaction between antigens and antibodies could be effectively enhanced in comparison with that in the conventional capacitive biosensors based on IDEs.

The total capacitance change (C_{total}) caused by the binding of analytes on the VPE was estimated to have the following relation: $C_{total} = C_{para} + C_{Ab} + C_{Ag}$, where C_{para} represents the parasitic capacitance of VPE, C_{Ab} is the capacitance change after immobilization of the antibody layer, and C_{Ag} represents the capacitance change caused by the binding of target analytes (Castiello et al., 2019; Jung et al., 2014; Lee et al., 2018b). As the capacitance change should be correlated to the capacitance change owing to the binding of analytes (C_{Ag}), the parasitic capacitance (C_{para}) should be decreased to a value as low as possible to enhance sensitivity.

The parasitic capacitance (C_{para}) was determined to be reduced by changing the conformation of the VPE as a ring-shaped electrode (Lee et al., 2018b). This VPE was fabricated using Au and Pt metal electrodes, and etching was performed through a wet process (Huske et al., 2014; Lee et al. 2013, 2018b; Wolfrum et al., 2016). Such wet-etching process of metal electrodes often contaminated dielectric layer (parylene film) which resulted in unexpected connection of electrodes (Brennan et al., 2015; Takeuchi et al., 2005). To solve this problem, conductive polymer, such as poly(3,4-ethylenedioxythiophene)–poly(styrenesulfonate) (PEDOT:PSS) was used as an electrode material for the fabrication of VPEs. The PEDOT:PSS is a widely used organic-based conductive material owing to the simple coating process, electrochemical properties, and mechanical flexibility (Huang et al. 2020a, 2020b; Zeng et al., 2021). Because the PEDOT:PSS was homogeneously soluble in water, the electrodes of VPE could be made by spin-coating, and the electrodes of PEDOT:PSS could be dry-etched with far reduced contamination of electrode material. Additionally, the electrodes of PEDOT:PSS were analyzed to have similar electrochemical properties of carbon-based electrodes, such as a low double-layer capacitance (C_{dl}) and a high electron transfer rate (k_{ET}).

In this study, the sensitivity enhancement was achieved by increasing the number of VPE electrode pairs. The sensitivity enhancement was also achieved by decreasing the VPE electrode gap. Such an increase in sensitivity related to the number of electrode pairs and the electrode gap was estimated using a model analyte for the immunoassay. Additionally, a computer simulation was performed using VPEs with different numbers of electrode pairs and various VPE electrode gaps. The electrode was fabricated using a conductive polymer layer of PEDOT:PSS instead of Ag and Pt metal electrodes (Butina et al., 2019; Dauzon et al., 2019; Lee and Kim, 2018; Wan et al., 2019), and the VPE fabrication yield was effectively etched using a reactive dry etching process. Finally, a VPE with multiple electrode pairs was applied for SARS-CoV-2 NP detection (Bong et al., 2021; Pollock et al., 2021; Zhang et al., 2020). The VPE-based capacitive biosensor with immobilized anti-SARS-CoV-2 NP antibodies was applied for specific SARS-CoV-2 detection in viral cultures of SARS-CoV-2, SARS-CoV, MERS-CoV, and CoV-strain 229E.

2. Materials and methods

2.1. Materials

Chemical reactants such as PEDOT:PSS (product #655201), bovine serum albumin (BSA), and horseradish peroxidase (HRP) were purchased from Sigma Aldrich. The anti-HRP antibody was purchased from Abcam (Cambridge, UK). The photoresists (GXR 601 and ARP-3220) for the photolithography process were obtained from NM Tech (Jollanamdo, Korea). The SARS-CoV-2 Nucleoprotein (NP) was purchased from Genbody Inc. (Cheonan, Korea). Culture fluids of SARS-CoV-2, SARS-CoV, MERS-CoV, CoV-strain 229E, NATtrol™ SARS-CoV-2 stock, and NATtrol™ SARS-CoV-2 negative stock were purchased from Zeptometrix (Buffalo, NY, USA). The distilled water was purified water using Milli-Q from Merck Millipore (Burlington, MA, USA).

2.2. Fabrication of the VPE

The was fabricated on an Si-SiO_2 wafer via repeated deposition of PEDOT:PSS (200 nm) and parylene-C film (500 nm). The VPE fabrication procedure is shown in Fig. 1b: (1) Photoresist (GXR 601) was patterned as an inverse pattern on cleaned Si-SiO_2 wafer, and PEDOT:PSS was spin-coated on the photoresist pattern; (2) Photoresist was removed using acetone, and PEDOT:PSS was patterned (Working electrode 1, 200 nm); (3) Parylene-C was deposited on the substrate during the thermal process (determining the electrode gap step); (4) PEDOT:PSS was patterned (Working electrode 2, 200 nm); (5) processes (1)–(4) were repeated (determining the electrode pair step), and (6) the photoresist (ARP-3220) was patterned (10 μm) with a hole shape for the top layer etching mask, and (7) ICP-RIE etched using O_2 and CF_4 gas with a power of 200 W for the electrode surface exposure and silver paste wiring. The PEDOT:PSS cross-section exposed via ICP-RIE etching was set as the electrode surface. The 1st, 3rd, and 5th layers were wired with silver paste and determined as WE1; the 2nd, 4th, and 6th layers were set as WE2. The capacitance was measured between WE1 and WE2 using an IVIUM potentiostat (Eindhoven, Netherlands). The surface profiles of the deposited layers were analyzed using atomic force microscopy from Park systems (Suwon, Korea). The electrode gap (d) of VPE was controlled by the parylene-C thickness. The parylene-C thickness can be controlled to less than 1 μm. The number of VPE electrode pairs (N) was controlled by the number of repeated processes.

2.3. Capacitive measurement using VPEs

The impedance between WE1 (1st, 3rd, and 5th layers) and WE2 (2nd, 4th, and 6th layers) was measured using a potentiostat from IVIUM Technologies in the frequency range of 0.1 Hz–10^6 Hz at an amplitude potential of 10 mV. The measured impedance was converted to capacitance data using Z View software from Scribner Associates INC (NC, USA). The software automatically calculates the capacitance and Nyquist plot from impedance data by using the "Randle equivalent circuit" model. The "Randle equivalent circuit" consists of a double-layer capacitance (C_{dl}) and a series medium resistance (R_s) with a parallel charge transfer resistance (R_{ct}) and Warburg impedance (W_s), which describes the resistive and capacitive parameters at the interface between the electrode and the electrolyte. The protein adsorption on the electrode changes the capacitance, which makes the capacitive sensor applicable to diagnostic detection without any labeling by using the specific binding between the antigen and antibody.

2.4. Computer simulation of electrode properties

The optimized electrical properties of the VPEs were determined using finite element method-based COMSOL™ Multiphysics software. For the simulation, the VPE was designed using a 2D-rotation model and an electric current module in the frequency domain. The simulation was performed in the frequency range of 0.1 Hz–10^6 Hz with a fixed potential of 10 mV. The model consists of an electrode (PEDOT:PSS: $\sigma = 400\ S\ m^{-1}$, $\varepsilon = 1$) with 200 nm thickness, a dielectric layer (Parylene: $\sigma = 10^{-13}\ S\ m^{-1}$, $\varepsilon = 2$), and a buffer layer (PBS: $\sigma = 1.6\ S\ m^{-1}$, $\varepsilon = 80$). For the VPE optimization, two parameters were controlled.

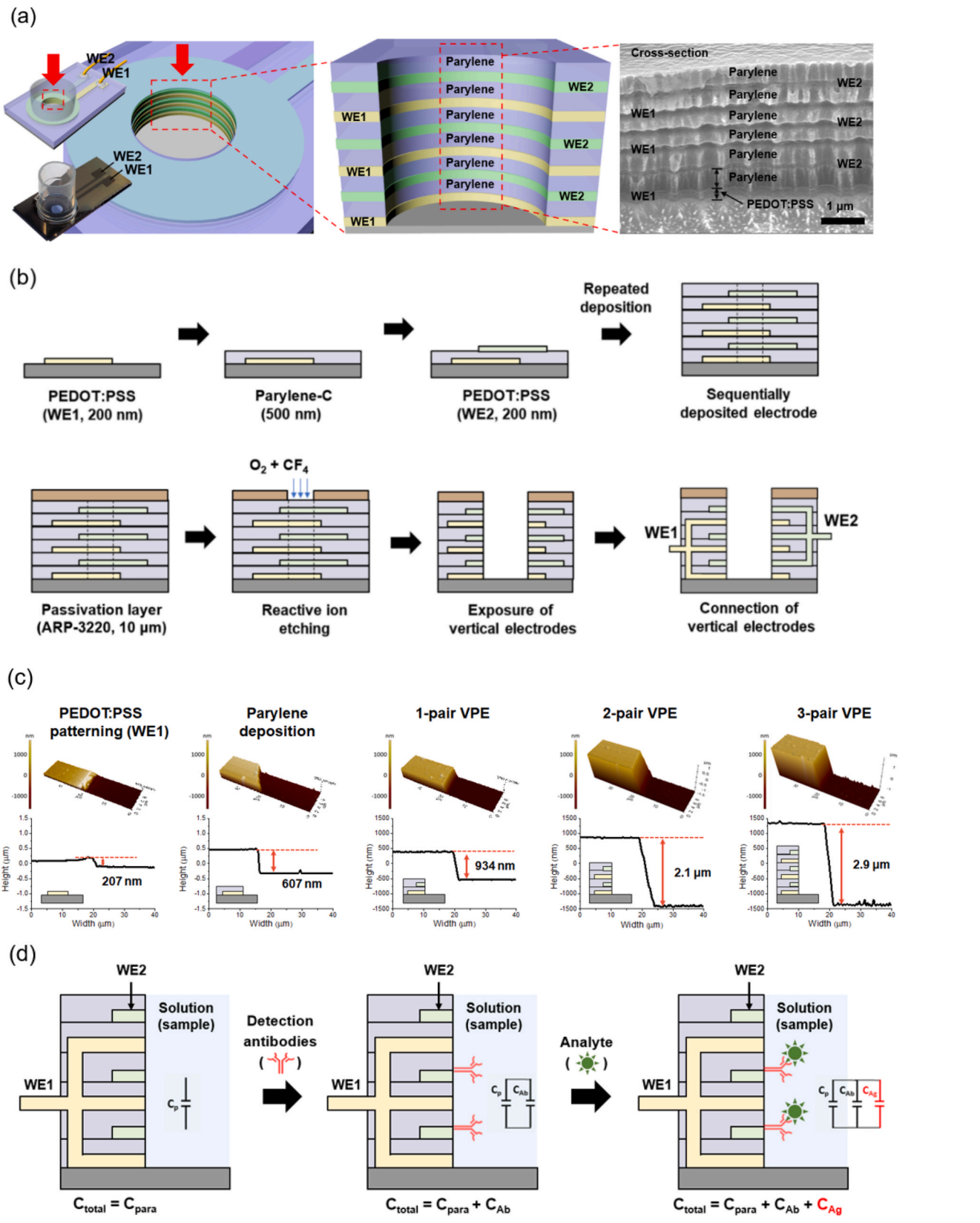

Fig. 1. Fabrication of vertically paired electrode (VPE) with three pairs of working electrodes (WE). (a) Structure of VPE and the SEM image of VPE. (b) Fabrication procedure of VPE. (c) AFM analysis of vertically paired electrodes with 1-, 2-, 3-paired electrodes. (d) Analog circuit of vertically paired capacitive biosensor for the detection of protein adsorption. The total capacitance change was measured from parasitic capacitance of electrode (C_{para}), capacitance changes from detection antibodies (C_{Ab}) and target analytes (antigens, C_{Ag}).

The first was the electrode gap between the electrode pairs (100–800 nm). The protein adsorption was realized using the surface impedance and the protein adsorption was defined as a thin film. The second was the number of electrode pairs (1–10 pairs). The antibody adsorption and antibody + antigen binding on the electrode surface were analyzed. The current distributions of the different VPE models were derived. From the current data, the capacitance was calculated using the following equations:

$$J = \sigma E + jwD + J_e \quad (1)$$

$$Z = \frac{V}{I} \quad (2)$$

$$Z = jwL + (iwC)^{-1} \quad (3)$$

$$C = -i(2\pi f \cdot Z)^{-1} \quad (4)$$

The current value of each frequency was calculated from the software using Eq. (1), where J represents the current density, J_e represents the externally generated current, E represents the electric field intensity, and D represents the electrical permittivity. The impedance (Z) can be calculated with the potential (V) fixed at 10 mV and the current value (I) from the software, as expressed in Eq. (2). As the inductor parameter (L) in the equivalent circuit is almost zero, Eq. (3) shows the relationship between impedance (Z) and capacitance (C). It is converted to Eq. (4), and the imaginary part of the impedance and the frequency were used for the capacitance calculation (Castiello et al., 2019).

2.5. Immunoassay with VPEs

For the application of a VPE to the diagnostic immunoassay, the immunoassay was performed using the VPE with HRP and anti-HRP antibody as a model protein. The anti-HRP antibody (10 μg mL-1, 100 μL) was immobilized for 2 h at 37 °C on the electrode, and HRP was incubated with various concentrations (between 10 ng mL-1 and 10 μg mL-1, 100 μL) for 30 min at 37 °C. After incubation, the electrode was washed with 1% Tween 20 and phosphate buffered saline (PBS) buffer (150 μL). The 1% PBS was selected as an electrolyte buffer to reduce the ion strength interference in the solution (Chu et al., 2017). For the diagnostic SARS-CoV-2 virus detection, the anti-NP of SARS-CoV-2 antibodies from pig sera was used for NP detection (Bong et al. 2019, 2021; Jung et al. 2021a, 2021b; Lee et al., 2019). The isolated antibodies were confirmed using SDS-PAGE gel. The binding affinity between the isolated antibody and SARS-CoV-2 was confirmed using a competitive assay. The specific affinity of antibodies against SARS-CoV-2 was tested using viral culture fluids of SARS-CoV2, SARS-CoV, MERS-CoV, and CoV-strain 229E (Bong et al., 2021; Jung et al., 2021a).

The isolated anti-NP antibodies were applied to one and three VPE pairs. The anti-NP antibody at a concentration of 10 μg mL^{-1} in 1% PBS (100 μL) was immobilized on the electrode surface for 2 h at 37 °C. The BSA (1 mg mL^{-1}, 100 μL) was used to block the electrode surface to reduce non-specific binding. After the blocking steps, NP samples were incubated with the VPE at concentrations ranging from 1 ng mL^{-1} to 1 μg mL^{-1} in 100 μL volume for 1 h at 37 °C. The capacitance was measured in the frequency range of 0.1–10 Hz. The capacitance change was calculated at 0.5 Hz. The VPEs with anti-NP antibody immobilization were used for the capacitive SARS-CoV-2 detection in the viral culture fluid. One and three VPE electrode pairs were used for viral culture fluid detection. The immobilization and blocking steps were the same as above, and the dilution factor of SARS-CoV-2 in viral culture was from 100–24,300 (1/3 serial dilution) for the standard curve.

The detection of other CoV strains in heat-inactivated viral culture fluid (SARS-CoV, MERS-CoV, and CoV-strain 229E) was analyzed using the same procedure as that for SARS-CoV-2 in viral culture fluid from Zeptometrix (Buffalo, NY, USA). According to the manufacturer's instruction, the median tissue culture infectious dose per milliliter ($TCID_{50}$/ml) of sample was estimated to be 3.09 x 10^8 for SARS-CoV-2, 3.55 x 10^8 for MERS-CoV, 1.41 x 10^8 for CoV strain 229E, and the cycle threshold (Ct) value of sample was in the range of 27.5–29.5 for SARS-CoV-2, 25–28 for SARS-CoV, MERS-CoV, CoV strain 229E.

The assay results of the presented capacitive biosensor were compared with a commercially available COVID-19 Ag test kit from SD biosensor (Suwon, Korea). According to the manufacturer's instruction, the test kit was certified to have indicated 82.5% sensitivity and performed 100% specificity for the patients' samples (n=145). And the cutoff value for the determination of positive samples was made by the 800-fold diluted viral culture of SARS-CoV-2 which could be correlated to the dilution factor of 0.13%. As real samples, chemically modified SARS-CoV-2 intact virus (for nucleic acid testing control, NATtrol ™ SARS-CoV-2 stock) from Zeptometrix (Buffalo, NY, USA) was used by dilution with NATtrol™ SARS-CoV-2 negative stock. These reagents were developed as standards for molecular diagnostics testing and could be used as independent quality control materials. The matrix of these samples was described to contain antioxidants, buffer salts, preservatives, antibiotics, and matrix stabilizing fillers such as sugars (monosaccharides and polysaccharides), proteins (including albumin, ovalbumin, gamma globulin, red blood cell lysates). The dilution factor was provided in percentage of the undiluted culture fluid: dilution factor (vol/vol, %) = SARS-CoV-2 stock/(SARS-CoV-2 stock + SARS-CoV-2 negative stock).

3. Results and discussion

3.1. Fabrication and properties of VPEs

The IDE has been used for the analysis of capacitive changes that occur owing to the protein adsorption on IDEs (Jung et al., 2014; Lee et al., 2018a; Luka et al., 2019; Quoc et al., 2019). Usually, an IDE is composed of serially connected capacitors comprising electrodes and dielectric layers between electrodes. The capacitive change in IDE is proportional to the electrode area and 1/electrode gap (Ghobaei Namhil et al., 2019; Jeon et al., 2014; Jung et al., 2014; Lee et al., 2018b; Sathya et al., 2019; Singh et al., 2011). Such IDEs were fabricated using photolithography, and the electrode gap was limited to a few micrometers using lab-based photolithography. To enhance the sensitivity of capacitive measurements using IDEs, the electrode gap needs to be reduced to less than 1 μm, and expensive fabrication processes are required. Recently, a VPE was developed for the fabrication of sensitive capacitive biosensors with electrode distances of less than 1 μm (Jung et al., 2014; Lee et al., 2018b; Sathya et al., 2019). In this study, the VPE was fabricated by spin-coating PEDOT:PSS at a thickness of 200 nm and a parylene film as dielectric layers at a thickness of 500 nm. As the VPE had a donut-shaped electrode, a cylindrical zone was created for the contact between the cross-sectional electrode surfaces and the sample fluid, as shown in Fig. 1a. The SEM image of the fabricated VPE shows the PEDOT:PSS electrode and parylene layers.

The cross-sectional VPE view after the RIE process showed three electrode pairs consisting of six electrodes on the substrate. The thickness of the PEDOT:PSS electrode layers was estimated to be 237.6±11.0 nm (n = 6), and those of the parylene layers were estimated to be 466.3±16.1 nm (n = 6). These results show that multiple VPEs can be fabricated using sequential deposition and etching processes for PEDOT:PSS electrodes and parylene films.

For VPE fabrication, the electrodes, and dielectric layers of the parylene film were sequentially deposited on the substrate, and multiple electrodes were fabricated by repeating this layering process. As shown in Fig. 1b, the cross-sectional electrode surface of the VPE was exposed by an etching process. In this study, a conducting polymer, PEDOT:PSS, was used as the electrode material (Butina et al., 2019; Dauzon et al., 2019; Wan et al., 2019). The PEDOT:PSS can easily be layered for electrode fabrication, and the cross-sectional VPE electrode surface can be developed via a reactive-ion etching (RIE) process. In the case of Au

or Pt metal electrodes, the sputtering process damages the parylene layers. Fine dust is generated and adsorbed on the dielectric layers, which causes unexpected shorts between the electrodes (Brennan et al., 2015; Gabriel, 1999; Takeuchi et al., 2005). Finally, the alternating electrode layers were connected for capacitive measurements. The thickness of the fabricated VPE was analyzed using AFM. As shown in Fig. 1c, the electrode of spin-coated PEDOT-PSS was estimated to be 207 nm and the dielectric layer of parylene film was deposited to be 607 nm. The fabricated VPE had the thickness of 934 nm for 1-pair, 2.1 μm for 2-pair and 2.9 μm for 3-pair electrodes.

For the capacitance measurement, the sample was contacted with the exposed electrode in the VPE cylindrical zone. This caused the VPE to acquire the parasitic capacitance (C_{para}) before the contact or the electrode analyte adsorption. For the immunoassay, the antibody layer was first immobilized on the electrode, and the analyte (antigen) was bound to the antibody layer. The antibody layer and analyte binding caused changes in C_{Ab} and C_{Ag}, respectively. As shown in Fig. 1d, the capacitive change on the cross-sectional VPE surface was correlated to the number of electrode pairs (N), dielectric constant (ε), electrode thickness (T_{th}), electrode radius (r), and electrode gap (d). The capacitance elements are considered to be parallel connected on the electrode, and the total capacitive change c can be obtained as their sum: $C_{total} = C_{para} + C_{Ab} + C_{Ag}$ (Castiello et al., 2019; Jung et al., 2014; Lee et al., 2018a).

The electrochemical properties of the PEDOT:PSS electrode were analyzed, such as the double-layer capacitance (C_{dl}), apparent rate constant for electron transfer (k_{ET}), and ideally polarizable potential range (electrochemical window). The double-layer capacitance was estimated from the charging current (non-faradaic current) on the electrode surface; PBS was used to avoid the overwhelming faradaic current from the redox couple (Garrett et al., 2012; Park et al., 2019). The current of the cyclic voltammogram is $i = C \bullet (dV/dt)$, where i is the current, C is the capacitance, and the capacitance corresponds to the plot slope of the current series magnitudes of cyclic voltammograms at a given potential (0 V in this study). As shown in Fig. 2a, the cyclic voltammograms were composed of oxidative and reductive waves, and the double-layer capacitance of the PEDOT:PSS electrode was estimated to be 10.3 μF cm^{-2} from the oxidative waves of the cyclic voltammograms. For carbon and metal electrodes, the double-layer capacitance values are reported as follows: diamond-like carbon (DLC) = 3.45 μF cm^{-2}, highly oriented pyrolytic graphite = 1–5 μF cm^{-2}, SiC = 3.75 μF cm^{-2}, Au = 30.9 μF cm^{-2}, Pt = 64.2 μF cm^{-2}, Ag = 52.8 μF cm^{-2}, and stainless steel = 39.8 μF cm^{-2} (Park et al., 2019). Usually, the double-layer capacitance of C-based electrodes is lower than that of metal electrodes, such as graphite (1–5 μF cm^{-2}) and DLC (3.45 μF cm^{-2}).

These results indicate that the PEDOT:PSS electrode has a double-layer capacitance in a range similar to those of carbon electrodes and significantly lower than those of metal electrodes. The apparent electron transfer rate constant (k_{ET}) was estimated for the PEDOT:PSS electrode in a redox coupling of 50 mM potassium ferricyanide and 1 M KCl using the Nicholson method (Park et al., 2019). In this method, the rate constant for electron transfer can be measured using cyclic voltammetry. As shown in Fig. 2b, the apparent rate constant for electron transfer (k_{ET}) of the PEDOT:PSS electrode was calculated to be 0.0013 cm s^{-1} from the peak potential separation ($\Delta E_p = E_a$-E_c) between the cathodic and anodic peaks in the cyclic voltammograms at different scan rates. Usually, metal electrodes exhibit fast electron transfer kinetics for many redox systems, and the rate constants for the electron transfer of Au and Pt are Au = 0.07–0.10 and Pt = 0.21 cm s^{-1} (Kim et al., 2011; Park et al., 2019). The rate constants for electron transfer (k_{ET}) of Carbon electrodes are lower than that for metal electrodes, such as glassy carbon = 0.0066, graphite = 10^{-6}, and DLC = 0.012 cm s^{-1} (Kneten and Mccreery, 1992). These results indicate that the PEDOT:PSS electrode (0.0013 cm s^{-1}) has a rate constant for electron transfer (k_{ET}) in a range similar to those of typical carbon-based electrodes. For electrochemical analysis, the ideal working electrode material is inert to redox reactions over a wide potential range, which is called the electrochemical window (Park et al., 2019). For the PEDOT:PSS electrode, the electrochemical window was measured to be −1.5–2.0 V versus an Ag/AgCl reference electrode, as shown in Fig. 2c. Such a wide electrochemical window indicates that the PEDOT:PSS electrode can be used as an ideally polarizable electrode for the electrochemical analysis of various target analytes, especially when high redox potentials are required.

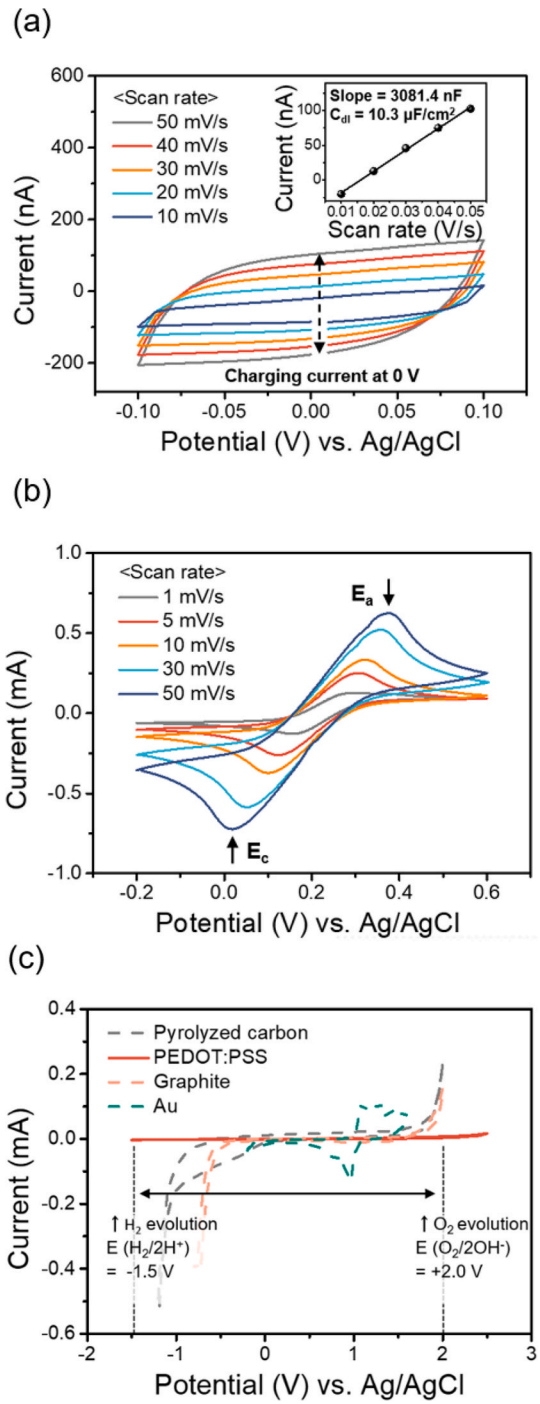

Fig. 2. Electrochemical properties of PEDOT:PSS electrode. (a) Cyclic voltammograms of PEDOT:PSS electrode at different scan rates under PBS for the double-layer capacitance (C_{dl}) estimation. (b) Electron transfer rate constant in a 50 mM potassium ferricyanide and 1 M KCl from the separation of cathodic (E_c) and anodic peaks (E_a) of cyclic voltammograms according to the scan rate. (c) Electrochemical windows of PEDOT:PSS electrode in 1 M H_2SO_4 compare to different materials.

3.2. Analysis of protein adsorption on VPEs

The VPE capacitance change was measured according to samples with different dielectric constants, such as air ($\varepsilon = 1$), distilled water ($\varepsilon = 80$), and PBS ($\varepsilon = 80$). The capacitance profile was measured in the frequency range of 0.1–10^4 Hz for three sample types (Fig. S1). Three VPE types with single-pair electrodes were prepared by changing the electrode gap (parylene film thickness) to 310, 610, and 860 nm. For each sample, the capacitance change was observed at a frequency of 0.5 Hz because the capacitive change was the most sensitively measured at this frequency for PBS. For the samples from the Air and DW, the change was observed to be nearly similar over a wide frequency range. The capacitance change was observed to be proportional to 1/distance for the three sample types. Such capacitive change trends were plotted together, and PBS was observed to induce significantly larger capacitive change in comparison with distilled water for the same electrode distances, as shown in Fig. 3a. From these results, the capacitive measurement conditions were determined to correspond to a frequency of 0.5 Hz in PBS as a buffer, and the VPE was prepared to have an electrode gap of less than 500 nm.

The capacitance change according to the protein adsorption was estimated using a VPE with different electrode gaps. As shown in Fig. 3b, HRP in PBS was coated on the VPE with a single pair of electrodes, and the electrode gap was controlled to be 310, 610, and 860 nm.

The capacitance was measured before and after HRP coating in the frequency range of 0.1–10 Hz, and the HRP adsorption was effectively monitored in the low-frequency range of less than 1 Hz (Kang et al., 2014; Le et al., 2020). The influence of the number of electrode pairs on the capacitive measurement was estimated using VPEs with one, two, and three electrode pairs. As shown in Fig. 3c, three types of VPEs were prepared with an electrode gap of 500 nm, and the capacitance was measured before and after HRP coating in the frequency range of 0.1–10 Hz. When the capacitance change was compared at a frequency of 0.5 Hz for the three VPE types, the VPE capacitance change before the HRP coating increased as the number of electrode pairs was increased. These results shows that the protein adsorption could be effectively measured using a VPE with a larger number of electrode pairs.

The charge transfer resistance (R_{ct}) was also estimated for the VPEs with one, two, and three electrode pairs using HRP as a model protein. A Nyquist plot was constructed for the three electrode types before and after HRP coating. As shown in Fig. 3d, the R_{ct} value was decreased from 18.6 to 4.6 kΩ for the VPE with a single electrode pair. The R_{ct} value was decreased from 5.8 (3.8) to 2.1 (1.1) kΩ for the VPE with two (three) electrode pairs. The change in R_{ct} values owing to HRP adsorption was estimated to be 14, 3.7, and 2.6 kΩ for the VPEs with one, two, and three electrode pairs, respectively. These results show that the change in R_{ct} values decreased with an increase in the number of electrode pairs. The decrease in R_{ct} values owing to the increase in the number of electrode pairs was considered to be owing to the increase in the area of electrodes with analytes.

The capacitive change for the immunoassay was estimated using VPEs with one, two, and three electrode pairs. When the VPE was in contact with the buffer, the capacitance corresponded to the parasitic capacitance (C_{para}) before the contact or electrode analyte adsorption. The antibody layer (anti-HRP antibodies) and analyte (HRP) binding caused changes in C_{Ab} and C_{Ag}, respectively. When the immunoassay was performed using VPEs with one, two, and three electrode pairs, the capacitance was measured for different HRP concentrations in the range of 10 ng mL^{-1}–10 μg mL^{-1} and the frequency range of 0.1–10 Hz, as shown in Fig. 4a. As the number of electrode pairs increased, the capacitive change increased. When the capacitance change of each sample at a frequency of 0.5 Hz from the value according to HRP adsorption was plotted together, as shown in Fig. 4b, the HRP detection sensitivity was estimated to be 47 nF/(ng/mL) for the VPE with a single electrode pair. The VPE sensitivities with two and three electrode pairs were estimated to be 115 nF/(ng/mL) and 233 nF/(ng/mL),

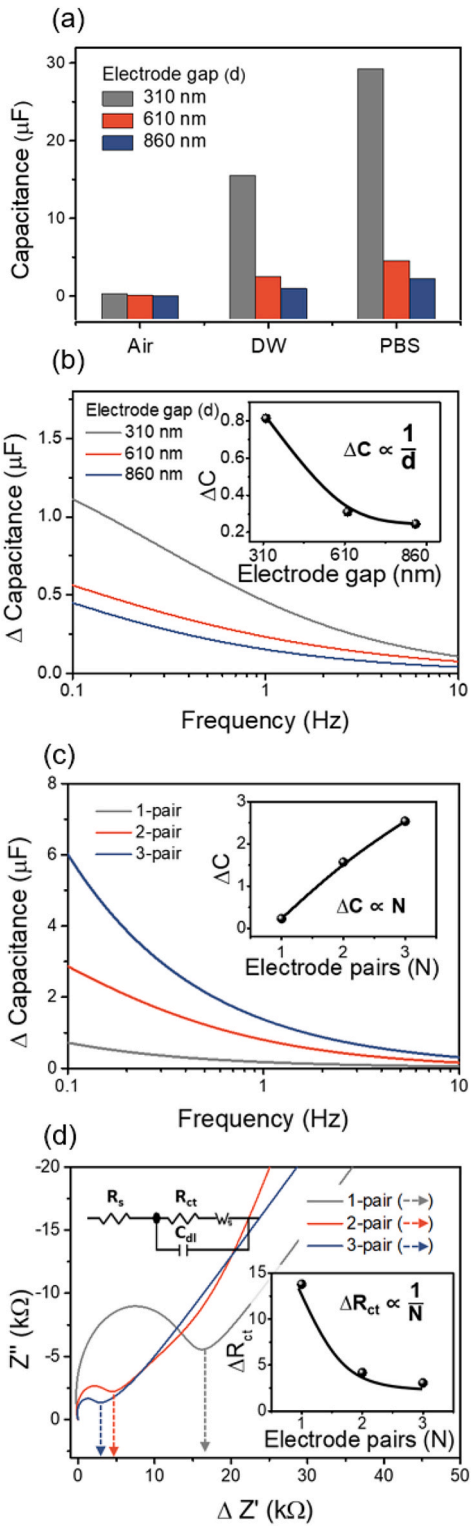

Fig. 3. Influencing factors for the capacitive measurement with VPE electrodes. (a) Electrode gap influence between two VPEs on the capacitance of different dielectric electrolytes of air, distilled water (DW) and phosphate-buffered saline (PBS). (b) Electrode gap influence on capacitance difference with the adsorption of model protein (HRP). (c) Influence of electrode pair numbers on capacitance difference with the adsorption of model protein (HRP). (d) Influence of electrode pair numbers on charge transfer resistance (R_{ct}) with the adsorption of model protein (HRP). The analog circuit consisted of resistance of solution (R_s), double-layer capacitance (C_{dl}), Warburg impedance (W_s) which represent the diffusion impedance in the low frequency and charge transfer resistance (R_{ct}).

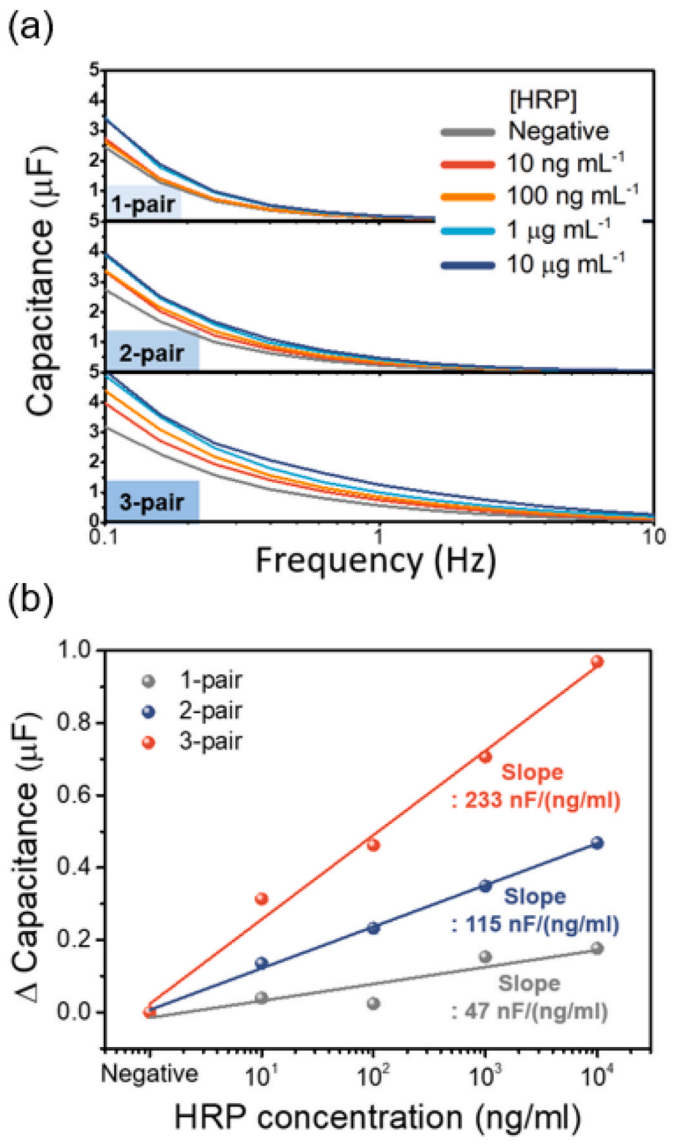

Fig. 4. Immunoassay with VPE electrode using model antigen-antibody interaction. (a) Capacitive measurement on sequential adsorption of anti-HRP antibodies and HRP model protein by using different electrode pairs. (b) Capacitive signal comparison between the different paired electrodes at a fixed frequency of 0.5 Hz.

respectively. These results indicate that the capacitance change was observed to increase with (1) increased analyte (HRP) concentration and (2) increased number of VPE electrode pairs.

To analyze the VPE properties according to the electrode gap and the number of electrode pairs, computer simulations were performed using commercial simulation software (COMSOL Multiphysics) (Castiello et al., 2019; Ha et al., 2019; Jung et al., 2014; Lee et al., 2018a). As shown in Fig. 5a, the electrode model was prepared for VPE using the conductivity (σ) and dielectric constant (ε) of the electrode (PEDOT:PSS, $\sigma = 400$ S m^{-1}, $\varepsilon = 1$) and parylene film ($\sigma = 10^{-12}$ S m^{-1}, $\varepsilon = 3$). The electrolyte was set to be PBS ($\sigma = 1.6$ S m^{-1}, $\varepsilon = 80$), and the protein layer was considered to be formed on the VPE electrode surface.

As shown in Fig. 5b, the protein in PBS was coated on the VPE with a single electrode pair, and the electrode gap was set to 100, 300, 500, and 800 nm. The VPEs with smaller distances between electrodes demonstrated a far higher electron density on the electrode surface. The capacitance change was calculated before and after protein coating in the frequency range of 0.1–10 Hz, and the capacitance change was

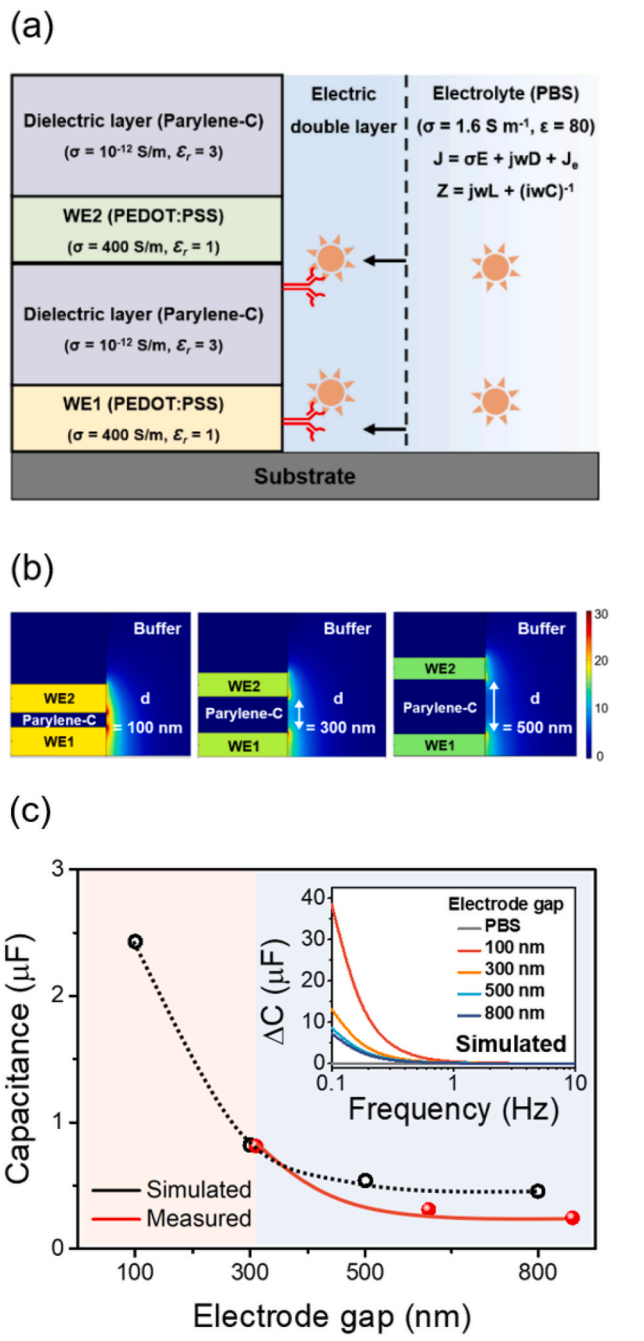

Fig. 5. Computer simulation for VPE optimization of the electrode gap. (a) Model of VPE finite element method. (b) Result of different electrode gaps for computer simulation of current distribution. (c) Comparison of simulation and measured results for different electrode gaps.

observed to increase as the distance between the electrodes decreased (inset of Fig. 5c). When the capacitance change was compared at a frequency of 0.5 Hz for the four VPE types, the capacitance changes steeply increased as the electrode gap decreased, as shown in Fig. 5c. These results demonstrated that the protein adsorption could be measured far more sensitively as the electrode gap was decreased. Although an electrode gap of 100 nm could not be fabricated in this study, the VPE with such a small electrode distance could achieve sensitive protein adsorption detection.

The VPE models with one, two, and three electrode pairs were also used for the immunoassay. As shown in Fig. 6a, an antibody layer and analyte (antigen) layer are formed on the VPE. As the number of

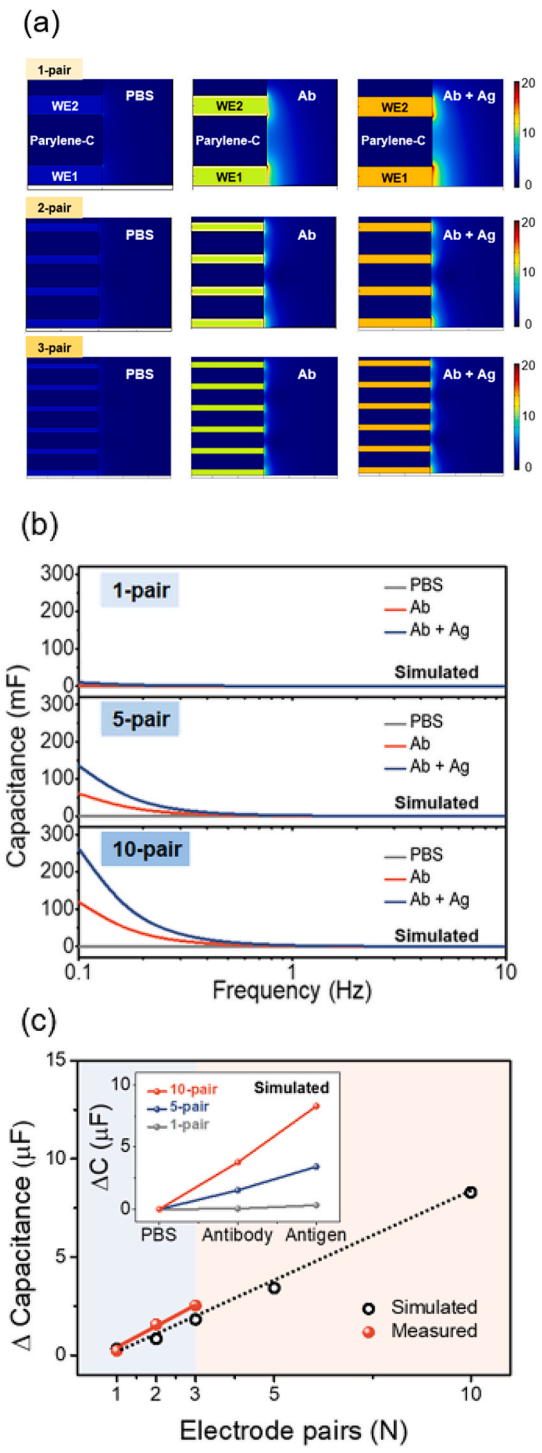

Fig. 6. Computer simulation for immunoassay with VPE using model antibody (Ab) – antigen (Ag) interaction. (a) Result of different electrode pairs for computer simulation of current distribution. (b) Capacitive measurement with different VPE pairs for protein adsorption (1–10 pairs). (c) Comparison of simulated and measured results for different electrode pairs.

electrode pairs increased, the current density on individual electrodes was observed to increase when antibody and antibody + antigen layers were formed on the electrodes, as shown in Fig. 6b. When antibody and antibody + antigen layers were formed on the electrode, the capacitance in the frequency range of 0.1–10 Hz was simulated for VPEs with one, two, and three electrode pairs. The capacitance increased steeply with an increase in the number of electrode pairs (inset of Fig. 6c). The capacitance difference before and after the adsorption of antibodies and antigens was observed in the low frequency range.

When the capacitance change was compared at a frequency of 0.5 Hz for five VPE types with various numbers of electrode pairs, the capacitance change was linearly proportional to the electrode pairs, as shown in Fig. 6c. These results demonstrated that the antigen + antibody immunoassay was more sensitive as the number of electrode pairs was increased. Although the five and ten electrode pair configurations were difficult to fabricate in this study, VPEs with such a large number of electrode pairs could realize very sensitive antigen/antibody immunoassay.

3.3. Application of VPEs

Coronavirus (CoV) has been known to have four genera: alpha-, beta-, gamma-, and delta-CoV strains, and beta-CoV have been reported to cause acute respiratory syndromes such as COVID-19. These CoVs develop four major protein types called nucleoprotein (NP), envelope protein, membrane protein, and spike protein, and NP has been frequently used for the diagnosis and development of vaccines.

Recently, the NP of beta-CoV strains that infected pigs was found to have a high amino acid sequence homology (>40%) with the amino acid sequence of SARS-CoV-2 NP (Bong et al., 2021; Pollock et al., 2021; Zhang et al., 2020). The anti-NP of SARS-CoV-2 antibodies was reported to be isolated from pig sera with pig immunization with NP as an antigen (Fig. S2a and Fig. S2b). Additionally, the isolated anti-NP of SARS-CoV-2 antibodies from pig sera could be used for the SARS-CoV-2 NP detection as well as for the SARS-CoV-2 immunoassay in the viral culture fluid. The cross-reactivities of the sensor was evaluated with other CoV strains viral culture fluids (SARS-CoV, MERS-CoV, and CoV-strain 229E) (Fig. S2c and Fig. S2d). In this study, the anti-NP of SARS-CoV-2 antibodies was isolated from pig sera, and the VPE was applied for SARS-CoV-2 NP detection.

First, anti-NP antibodies were immobilized on the VPEs with one and three electrode pairs. After blocking the sites for non-specific binding with BSA, the NP samples were treated with VPEs for capacitive measurement.

As shown in Fig. 7a, anti-NP antibodies were immobilized on the VPEs with one and three electrode pairs for standard NP samples in the concentration range of 1 ng mL $^{-1}$–1 μg mL^{-1}. The capacitance was measured in the frequency range of 0.1–10 Hz, and the VPE with three electrode pairs demonstrated a far higher capacitance change than the single pair VPE. As shown in Fig. 7b, the standard curve from the VPE with three electrode pairs demonstrated far higher sensitivity than that from the VPE with a single electrode pair. The VPEs with immobilized anti-NP antibodies were used to detect SARS-CoV-2 in the viral culture fluid. As shown in Fig. 7c, the VPE with a single electrode pair could be used for the quantitative SARS-CoV-2 detection in viral culture fluid at a dilution factor range of 100–24,300 (1/3 serial dilution), and the detection limit was estimated to be a dilution factor of 0.04%. When other CoV strains in viral culture fluids were analyzed using the VPEs with immobilized anti-NP antibodies, the sensitivity was observed to be far higher for SARS-CoV-2 than for SARS-CoV, MERS-CoV, and CoV-strain 229E. Considering the cutoff for the SARS-CoV-2 detection in viral fluid to be 0.13% (dilution factor of 1/800 which corresponds to 147 $TCID_{50}$/mL) from a previous report (Bong et al., 2021; Jung et al., 2021a), these results demonstrated that a VPE with a single electrode pair could be effectively used for SARS-CoV-2 detection in viral fluid. As shown in Fig. 7c, the VPE with three electrode pairs was used for quantitative SARS-CoV-2 detection in viral culture fluid at a dilution factor range of 100–24,300 (1/3 serial dilution), and the detection limit was estimated to be a dilution factor of 0.01%. Other CoV strains in viral culture fluids were analyzed using VPE electrodes with immobilized anti-NP antibodies, and the sensitivity was also observed to be far higher for SARS-CoV-2 than for SARS-CoV, MERS-CoV, and CoV-strain 229E. The sensitivity was estimated to be four times higher than that of the

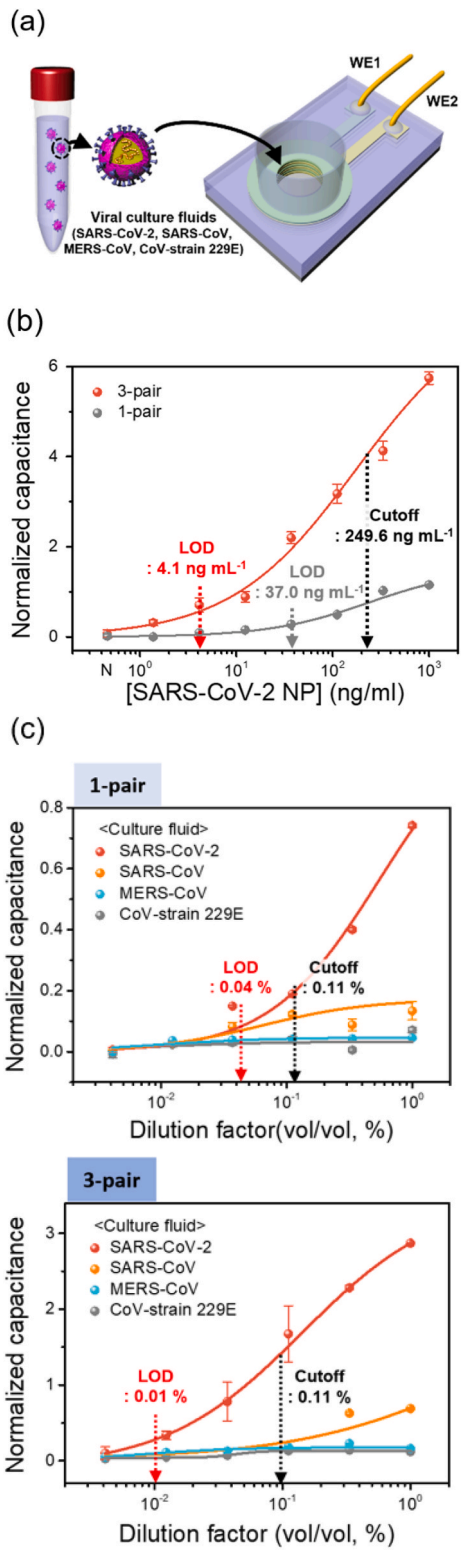

Fig. 7. Application of VPE to SARS-CoV-2 detection in viral fluids. (a) Schematic view of the immunoassay for viral culture fluids. (b) Anti-SARS-CoV-2 NP capacitive immunoassay result on VPEs with different electrode pairs. (c) Immunoassay result on VPEs for four CoV viral culture fluid types using the anti-SARS-CoV-2 NP antibodies and 1 and 3 VPE pairs.

VPE with only one electrode pair.

The assay results of the capacitive biosensor were compared with a commercially available COVID-19 Ag rapid test kit from SD biosensor (Suwon, Korea). As the first step, the standard curve for the analysis of real samples of SARS-CoV-2 (NATtrol™ SARS-CoV-2 stock diluted with NATtrol™ SARS-CoV-2 negative stock) was prepared as shown in Fig. 8a.

As the standard real samples, NATtrol™ SARS-CoV-2 stock that contains an intact virus in the specific matrix is widely used (Parker et al., 2020; Pickering et al., 2021), and the matrix of NATtrol™ samples was made to contain antioxidants, buffer salts, preservatives, antibiotics, and matrix stabilizing fillers such as sugars, proteins that mimic the composition of clinical sample (Chan et al., 2016; Eboigbodin et al., 2016; Favaro et al., 2021). And then, the assay results were compared

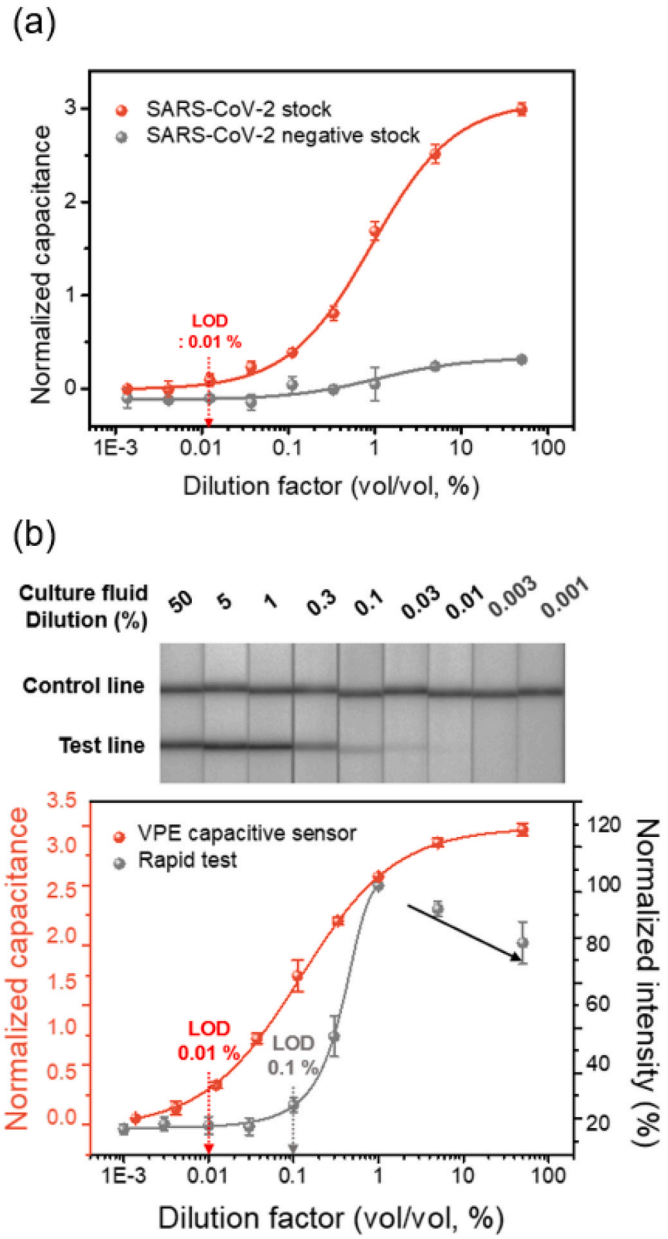

Fig. 8. Analysis of real samples of SARS-CoV-2 (NATtrol™ SARS-CoV-2 stock diluted with NATtrol™ SARS-CoV-2 negative stock) in comparison with a commercial rapid test kit. (a) Standard curve for the detection of SARS-CoV-2 in NATtrol™ SARS-CoV-2 stock diluted with NATtrol™ SARS-CoV-2 negative stock. (b) Comparison of assay results between the capacitive biosensor and the commercial rapid test.

with a commercially available rapid test kit. As shown in Fig. 8b, the limit of detection (LOD) was estimated to be 0.1% for the rapid test kit and 0.01% for the capacitive biosensor. The detection range was estimated to be 0.1–1.0% for the rapid test kit and 0.01–50% for the capacitive biosensor. The cutoff level of SARS-CoV-2 is reported to be 50–400 PFU/mL (Pickering et al., 2021), 100–200 $TCID_{50}$/mL (Hartard et al., 2021), and the Ct cutoff of 35–40 cycles (Morehouse et al., 2021). In this work, the validity of the rapid test was confirmed from the instruction from the manufacturer. The limit of detection (LOD) value of the rapid test kit was estimated to be the dilution factor of 0.10% (1000-fold dilution) as shown in Fig. 8b, and the cutoff value from the manufacturer was the dilution factor of 0.13% (800-fold dilution), which corresponds to 147 $TCID_{50}$/mL. In comparison with the reported cutoff level of SARS-CoV-2, these results showed that the calculated cutoff value is valid to medical diagnosis. Additionally, the rapid test showed Hook effect at the higher concentration of more than 1%. These results showed that the capacitive biosensor could detect SARS-CoV-2 with significantly high sensitivity and a wider detection range in comparison with the commercially available rapid test. These results demonstrated that the VPE with three electrode pairs could be more effectively used for SARS-CoV-2 detection in the viral fluid.

4. Conclusion

A VPE with multiple electrode pairs was fabricated using a conducting polymer, PEDOT:PSS as the electrode material, and a parylene film dielectric layer. The VPE capacitance change was measured according to samples with different dielectric constants, such as air ($\varepsilon = 1$), distilled water ($\varepsilon = 80$), and PBS ($\varepsilon = 80$), and the capacitive measurement conditions were determined to correspond to a frequency of 0.5 Hz in PBS as a buffer, and the VPE was prepared to have an electrode gap of less than 500 nm. The capacitance change according to protein adsorption was estimated using VPEs with different electrode gaps, and the protein adsorption could be effectively measured using VPEs with an electrode gap of less than 500 nm at a fixed frequency of 0.5 Hz.

The influence of the number of electrode pairs on the capacitive measurement was estimated using VPEs with one, two, and three electrode pairs as well as a VPE with an electrode gap of less than 500 nm and a large number of electrode pairs. When the VPE was in contact with the buffer, the capacitance corresponded to the parasitic capacitance (C_{para}) before the contact or electrode analyte adsorption. The antibody layer (anti-HRP antibodies) and analyte (HRP) binding caused changes in C_{Ab} and C_{Ag}, respectively. The capacitance change was observed to increase with (1) increased analyte (HRP) concentration and (2) increased numbers of VPE electrode pairs. To analyze the VPE properties according to the electrode gap and the number of electrode pairs, computer simulations were performed using commercial simulation software. These simulation results are consistent with empirical data showing that the capacitance change owing to the analyte adsorption was observed to increase when (1) the electrode gap decreased and (2) the number of VPE electrode pairs increased. Finally, the anti-NP of SARS-CoV-2 antibodies was isolated from pig sera, and VPE was applied for SARS-CoV-2 NP detection. The VPE with three electrode pairs was used for the quantitative SARS-CoV-2 detection in viral culture fluid at a dilution factor range of 100–24,300 (1/3 serial dilution), and the detection limit was estimated to be a dilution factor of 0.01%, which was 10 times more sensitive than the cutoff value. The sensitivity was also observed to be far higher for SARS-CoV-2 in comparison with other CoV strains in viral culture fluids analyzed using the VPEs with immobilized anti-NP antibodies, such as SARS- CoV, MERS-CoV, and CoV-strain 229E, and the assay results from the capacitive biosensor were compared with commercial rapid kit based on a lateral flow immunoassay.

CRediT authorship contribution statement

Jun-Hee Park: Experiment, Data curation, Writing – original draft. **Ga-Yeon Lee:** Experiment, Data curation. **Zhiquan Song:** Experiment, Data curation. **Ji-Hong Bong:** Experiment, Data curation. **Young-Wook Chang:** Experiment, Data curation. **Sungbo Cho:** Validation, Supervision. **Min-Jung Kang:** Validation, Supervision. **Jae-Chul Pyun:** Supervision, Funding acquisition, Writing – original draft, Writing – review & editing.

Declaration of competing interest

The authors declare that they have no known competing financial interests or personal relationships that could have appeared to influence the work reported in this paper.

Acknowledgment

This work was supported by the National Research Foundation of Korea (grant numbers: NRF-2020R1A2B5B01002187, NRF-2020R1A5A101913111 and NRF-2021R1A2C209370611).

Appendix A. Supplementary data

Supplementary data to this article can be found online at https://doi.org/10.1016/j.bios.2022.113975.

References

Ahn, J., Lee, T.H., Li, T., Heo, K., Hong, S., Ko, J., Kim, Y., Shin, Y.B., Kim, M.G., 2011. Electrical immunosensor based on a submicron-gap interdigitated electrode and gold enhancement. Biosens. Bioelectron. 26, 4690–4696.
Bong, J.H., Kim, J., Lee, G.Y., Park, J.H., Kim, T.H., Kang, M.J., Pyun, J.C., 2019. Fluorescence immunoassay of E. coli using anti-lipopolysaccharide antibodies isolated from human serum. Biosens. Bioelectron. 126, 518–528.
Bong, J.H., Kim, T.H., Jung, J., Lee, S.J., Sung, J.S., Lee, C.K., Kang, M.J., Kim, H.O., Pyun, J.C., 2021. Competitive immunoassay of SARS-CoV-2 using pig sera-derived anti-SARS-CoV-2 antibodies. Biochip J 15, 100–108.
Brennan, C.J., Neumann, C.M., Vitale, S.A., 2015. Comparison of gate dielectric plasma damage from plasma-enhanced atomic layer deposited and magnetron sputtered TiN metal gates. J. Appl. Phys. 118, 045307.
Butina, K., Loffler, S., Rhen, M., Richter-Dahlfors, A., 2019. Electrochemical sensing of bacteria via secreted redox active compounds using conducting polymers. Sensor. Actuator. B Chem. 297, 126703.
Castiello, F.R., Porter, J., Modarres, P., Tabrizian, M., 2019. Interfacial capacitance immunosensing using interdigitated electrodes: the effect of insulation/immobilization chemistry. Phys. Chem. Chem. Phys. 21, 15787–15797.
Chan, M., Jiang, B., Ng, S.Y., Tan, T.Y., 2016. Novel cost-effective quality control approach for the Cepheid Xpert CT/NG assay for the detection of Chlamydia Trachomatis and Neisseria Gonorrhoeae. J. Microbiol. Methods 125, 87–90.
Chen, J., Xue, F., Yu, Z., Huang, L., Tang, D., 2020. A polypyrrole-polydimethylsiloxane sponge-based compressible capacitance sensor with molecular recognition for point-of-care immunoassay. Analyst 145, 7186–7190.
Chen, J.L., Tong, P., Huang, L.T., Yu, Z.H., Tang, D.P., 2019. Ti3C2 MXene nanosheet-based capacitance immunoassay with tyramine-enzyme repeats to detect prostate-specific antigen on interdigitated micro-comb electrode. Electrochim. Acta 319, 375–381.
Chu, C.H., Sarangadharan, I., Regmi, A., Chen, Y.W., Hsu, C.P., Chang, W.H., Lee, G.Y., Chyi, J.I., Chen, C.C., Shiesh, S.C., Lee, G.B., Wang, Y.L., 2017. Beyond the Debye length in high ionic strength solution: direct protein detection with field-effect transistors (FETs) in human serum. Sci. Rep. 7, 5256.
Dauzon, E., Mansour, A.E., Niazi, M.R., Munir, R., Smilgies, D.M., Sallenave, X., Plesse, C., Goubard, F., Amassian, A., 2019. Conducting and stretchable PEDOT:PSS electrodes: role of additives on self-assembly, morphology, and transport. ACS Appl. Mater. Interfaces 11, 17570–17582.
Eboigbodin, K.E., Brummer, M., Ojalehto, T., Hoser, M., 2016. Rapid molecular diagnostic test for Zika virus with low demands on sample preparation and instrumentation. Diagn. Microbiol. Infect. Dis. 86, 369–371.
Favaro, M., Mattina, W., Pistoia, E.S., Gaziano, R., Di Francesco, P., Middleton, S., D'Angelo, S., Altarozzi, T., Fontana, C., 2021. A new qualitative RT-PCR assay detecting SARS-CoV-2. Sci. Rep. 11, 18955.
Fowler, J.D., Allen, M.J., Tung, V.C., Yang, Y., Kaner, R.B., Weiller, B.H., 2009. Practical chemical sensors from chemically derived graphene. ACS Nano 3, 301–306.
Gabriel, C.T., 1999. Gate oxide damage: testing approaches and methodologies. J. Vac. Sci. Technol., A 17, 1494–1500.

Garrett, D.J., Ganesan, K., Stacey, A., Fox, K., Meffin, H., Prawer, S., 2012. Ultra-nanocrystalline diamond electrodes: optimization towards neural stimulation applications. J. Neural. Eng. 9, 016002.
Ghobaei Namhil, Z., Kemp, C., Verrelli, E., Iles, A., Pamme, N., Adawi, A.M., Kemp, N.T., 2019. A label-free aptamer-based nanogap capacitive biosensor with greatly diminished electrode polarization effects. Phys. Chem. Chem. Phys. 21, 681–691.
Ha, M.T., Shin, Y.J., Bae, S.Y., Park, S.Y., Jeong, S.M., 2019. Effect of hot-zone aperture on the growth behavior of SiC single crystal produced via top-seeded solution growth method. J. Kor. Chem. Soc. 56, 589–595.
Hadiyan, M., Salehi, A., Mirzanejad, H., 2020. Gas sensing behavior of Cu2O and CuO/Cu2O composite nanowires synthesized by template-assisted electrodeposition. J. Kor. Chem. Soc. 58, 94–105.
Hartard, C., Berger, S., Josse, T., Schvoerer, E., Jeulin, H., 2021. Performance evaluation of an automated SARS-CoV-2 Ag test for the diagnosis of COVID-19 infection on nasopharyngeal swabs. Clin. Chem. Lab. Med. 59, 2003–2009.
Huang, L., Chen, J., Yu, Z., Tang, D., 2020a. Self-powered temperature sensor with seebeck effect transduction for photothermal-thermoelectric coupled immunoassay. Anal. Chem. 92, 2809–2814.
Huang, L.T., Yu, Z.H., Chen, J.L., Tang, D.P., 2020b. Pressure-based bioassay perceived by a flexible pressure sensor with synergistic enhancement of the photothermal effect. Acs Appl. Bio Mater. 3, 9156–9163.
Huske, M., Stockmann, R., Offenhausser, A., Wolfrum, B., 2014. Redox cycling in nanoporous electrochemical devices. Nanoscale 6, 589–598.
Jeon, D.Y., Park, S.J., Kim, Y., Shin, M.J., Kang, P.S., Kim, G.T., 2014. Impedance characterization of nanogap interdigitated electrode arrays fabricated by tilted angle evaporation for electrochemical biosensor applications. J. Vac. Sci. Technol. B 32, 021803.
Jung, H.W., Chang, Y.W., Lee, G.Y., Cho, S., Kang, M.J., Pyun, J.C., 2014. A capacitive biosensor based on an interdigitated electrode with nanoislands. Anal. Chim. Acta 844, 27–34.
Jung, J., Bong, J.H., Kim, H.R., Park, J.H., Lee, C.K., Kang, M.J., Kim, H.O., Pyun, J.C., 2021a. Anti-SARS-CoV-2 nucleoprotein antibodies derived from pig serum with a controlled specificity. Biochip J 15, 195–203.
Jung, J., Bong, J.H., Kim, T.H., Sung, J.S., Lee, C., Kang, M.J., Kim, H.O., Shin, H.J., Pyun, J.C., 2021b. Isolation of antibodies against the spike protein of SARS-CoV from pig serum for competitive immunoassay. Biochip J 15, 396–405.
Kang, J., Wen, J.Z., Jayaram, S.H., Yu, A.P., Wang, X.H., 2014. Development of an equivalent circuit model for electrochemical double layer capacitors (EDLCs) with distinct electrolytes. Electrochim. Acta 115, 587–598.
Kim, D.Y., Wang, J., Yang, J., Kim, H.W., Swain, G.M., 2011. Electrolyte and temperature effects on the electron transfer kinetics of Fe(CN)(6)(-3/-4) at boron-doped diamond thin film electrodes. J. Phys. Chem. C 115, 10026–10032.
Kim, H.R., Bong, J.H., Jung, J., Sung, J.S., Kang, M.J., Park, J.G., Pyun, J.C., 2020. An on-chip chemiluminescent immunoassay for bacterial detection using in situ-synthesized cadmium sulfide nanowires with passivation layers. Biochip J 14, 268–278.
Kim, H.R., Bong, J.H., Park, J.H., Song, Z., Kang, M.J., Son, D.H., Pyun, J.C., 2021. Cesium lead bromide (CsPbBr3) perovskite quantum dot-based photosensor for chemiluminescence immunoassays. ACS Appl. Mater. Interfaces 13, 29392–29405.
Kneten, K.R., Mccreery, R.L., 1992. Effects of redox system structure on electron-transfer kinetics at ordered graphite and glassy-carbon electrodes. Anal. Chem. 64, 2518–2524.
Le, H.T.N., Park, J., Cho, S., 2020. A probeless capacitive biosensor for direct detection of amyloid beta 1-42 in human serum based on an interdigitated chain-shaped electrode. Micromachines 11, 791.
Lee, G.Y., Bong, J.H., Kim, J.Y., Yoo, G., Park, M., Kang, M.J., Jose, J., Pyun, J.C., 2019. Thermophoretic diagnosis of autoimmune diseases based on Escherichia coli with autodisplayed autoantigens. Anal. Chim. Acta 1055, 106–114.
Lee, G.Y., Chang, Y.W., Ko, H., Kang, M.J., Pyun, J.C., 2016. Band-type microelectrodes for amperometric immunoassays. Anal. Chim. Acta 928, 39–48.
Lee, G.Y., Choi, Y.H., Chung, H.W., Ko, H., Cho, S., Pyun, J.C., 2013. Capacitive immunoaffinity biosensor based on vertically paired ring-electrodes. Biosens. Bioelectron. 40, 227–232.
Lee, G.Y., Park, J.H., Chang, Y.W., Cho, S., Kang, M.J., Pyun, J.C., 2018a. Chronoamperometry-based redox cycling for application to immunoassays. ACS Sens. 3, 106–112.
Lee, G.Y., Park, J.H., Chang, Y.W., Kang, M.J., Cho, S., Pyun, J.C., 2018b. Capacitive biosensor based on vertically paired electrode with controlled parasitic capacitance. Sensor. Actuator. B Chem. 273, 384–392.
Lee, H., Kim, J., 2018. Micro-cavity effect of ZnO/Ag/ZnO multilayers on green quantum dot light-emitting diodes. J. Kor. Chem. Soc. 55, 174–177.
Li, X., Batchelor-McAuley, C., Shao, L., Sokolov, S.V., Young, N.P., Compton, R.G., 2017. Quantifying single-carbon nanotube-electrode contact via the nanoimpact method. J. Phys. Chem. Lett. 8, 507–511.
Luka, G., Samiei, E., Dehghani, S., Johnson, T., Najjaran, H., Hoorfar, M., 2019. Label-Free capacitive biosensor for detection of cryptosporidium. Sensors 19, 258.
Minh, Q.N., Tong, H.D., Kuijk, A., van de Bent, F., Beekman, P., van Rijn, C.J.M., 2017. Gas sensing performance at room temperature of nanogap interdigitated electrodes for detection of acetone at low concentration. RSC Adv. 7, 50279–50286.
Morehouse, Z.P., Samikwa, L., Proctor, C.M., Meleke, H., Kamdolozi, M., Ryan, G.L., Chaima, D., Ho, A., Nash, R.J., Nyirenda, T.S., 2021. Validation of a direct-to-PCR COVID-19 detection protocol utilizing mechanical homogenization: a model for reducing resources needed for accurate testing. PLoS One 16, 0256316.
Park, J.H., Bong, J.H., Jung, J., Sung, J.S., Lee, G.Y., Kang, M.J., Pyun, J.C., 2021. Microbial biosensor for Salmonella using anti-bacterial antibodies isolated from human serum. Enzym. Microb. Technol. 144, 109721.
Park, J.H., Song, Z., Lee, G.Y., Jeong, S.M., Kang, M.J., Pyun, J.C., 2019. Hypersensitive electrochemical immunoassays based on highly N-doped silicon carbide (SiC) electrode. Anal. Chim. Acta 1073, 30–38.
Parker, C.W., Singh, N., Tighe, S., Blachowicz, A., Wood, J.M., Seuylemezian, A., Vaishampayan, P., Urbaniak, C., Hendrickson, R., Laaguiby, P., Clark, K., Clement, B. G., O'Hara, N.B., Couto-Rodriguez, M., Bezdan, D., Mason, C.E., Venkateswaran, K., 2020. End-to-End protocol for the detection of SARS-CoV-2 from built environments. mSystems 5, 720–771.
Pickering, S., Batra, R., Merrick, B., Snell, L.B., Nebbia, G., Douthwaite, S., Reid, F., Patel, A., Kia Ik, M.T., Patel, B., Charalampous, T., Alcolea-Medina, A., Lista, M.J., Cliff, P.R., Cunningham, E., Mullen, J., Doores, K.J., Edgeworth, J.D., Malim, M.H., Neil, S.J.D., Galao, R.P., 2021. Comparative performance of SARS-CoV-2 lateral flow antigen tests and association with detection of infectious virus in clinical specimens: a single-centre laboratory evaluation study. Lancet Microbe 2, 461–471.
Pollock, N.R., Savage, T.J., Wardell, H., Lee, R.A., Mathew, A., Stengelin, M., Sigal, G.B., 2021. Correlation of SARS-CoV-2 nucleocapsid antigen and RNA concentrations in nasopharyngeal samples from children and adults using an ultrasensitive and quantitative antigen assay. J. Clin. Microbiol. 59, 3020–3077.
Quoc, T.V., Ngoc, V.N., Bui, T.T., Jen, C.P., Duc, T.C., 2019. High-frequency interdigitated array electrode-based capacitive biosensor for protein detection. Biochip J 13, 403–415.
Santos-Neto, I.S.D., Carvalho, C.D., Filho, G.B.A., Andrade, C., Santos, G.C.O., Barros, A. K., Neto, J., Casas, V.L.P., Alencar, L.M.R., Lopes, A.J.O., Silva, F.C., Sinfronio, F.S. M., 2021. Interdigitated electrode for electrical characterization of commercial pseudo-binary biodiesel-diesel blends. Sensors 21, 7288.
Santschi, C., Jenke, M., Hoffmann, P., Brugger, J., 2006. Interdigitated 50 nm Ti electrode arrays fabricated using XeF2enhanced focused ion beam etching. Nanotechnology 17, 2722–2729.
Sathya, S., Muruganand, S., Manikandan, N., Karuppasamy, K., 2019. Design of capacitance based on interdigitated electrode for BioMEMS sensor application. Mater. Sci. Semicond. Process. 101, 206–213.
Singh, K.V., Bhura, D.K., Nandamuri, G., Whited, A.M., Evans, D., King, J., Solanki, R., 2011. Nanoparticle-enhanced sensitivity of a nanogap-interdigitated electrode array impedimetric biosensor. Langmuir 27, 13931–13939.
Song, Z., Im, J.H., Ko, H., Park, J.H., Lee, G.Y., Kang, M.J., Kim, M.H., Pyun, J.C., 2021. Plasma deposition of parylene-C film. Mater. Today Commun. 26, 101834.
Takeuchi, H., She, M., Watanabe, K., King, T.J., 2005. Damage-less sputter depositions by plasma charge trap for metal gate technologies. IEEE Trans. Semicond. Manuf. 18, 350–354.
Tang, D., Zhang, B., Liu, B., Chen, G., Lu, M., 2014. Digital multimeter-based immunosensing strategy for sensitive monitoring of biomarker by coupling an external capacitor with an enzymatic catalysis. Biosens. Bioelectron. 55, 255–258.
Wan, H.C., Cao, Y.Q., Lo, L.W., Xu, Z.H., Sepulveda, N., Wang, C., 2019. Screen-printed soft triboelectric nanogenerator with porous PDMS and stretchable PEDOT:PSS electrode. J. Semiconduct. 40, 112601.
Wolfrum, B., Katelhon, E., Yakushenko, A., Krause, K.J., Adly, N., Huske, M., Rinklin, P., 2016. Nanoscale electrochemical sensor arrays: redox cycling amplification in dual-electrode systems. Acc. Chem. Res. 49, 2031–2040.
Zeng, R.J., Wang, W.J., Chen, M.M., Wan, Q., Wang, C.C., Knopp, D., Tang, D.P., 2021. CRISPR-Cas12a-driven MXene-PEDOT:PSS piezoresistive wireless biosensor. Nano Energy 82, 105711.
Zhang, C., Zhou, L., Du, K., Zhang, Y., Wang, J., Chen, L., Lyu, Y., Li, J., Liu, H., Huo, J., Li, F., Wang, J., Sang, P., Lin, S., Xiao, Y., Zhang, K., He, K., 2020. Foundation and clinical evaluation of a new method for detecting SARS-CoV-2 antigen by fluorescent microsphere immunochromatography. Front Cell Infect Microbiol 10, 553837.